Electronic Supplementary Material

Two-dimensional conductive metal-organic frameworks as efficient electrocatalysts for oxygen evolution and reduction reactions

Yanan Zhou,[a] Li Sheng,[b] Lanlan Chen,[c] Qiquan Luo,[d] Wenhui Zhao,*[e] Wenhua Zhang,*[c] and Jinlong Yang*[f]

[a] *School of Material Science and Chemical Engineering, Institute of Mass Spectrometry, Ningbo University, Fenghua Road 818, Ningbo 315211, China*

[b] *Department of Chemical Physics, University of Science and Technology of China, Hefei, Anhui 230026, China*

[c] *Department of Material Science and Engineering, University of Science and Technology of China, Hefei, Anhui 230026, China. E-mail: whhzhang@ustc.edu.cn.*

[d] *Institutes of Physical Science and Information Technology, Anhui University, Hefei 230601, China*

[e] *Department of Physics, Ningbo University, Fenghua Road 818, Ningbo 315211, China. E-mail: zhaowenhui@nbu.edu.cn.*

[f] *Hefei National Laboratory for Physical Sciences at the Microscale, CAS Key Laboratory of Materials for Energy Conversion and Synergetic Innovation Centre of Quantum Information and Quantum Physics, University of Science and Technology of China, Hefei, Anhui 230026, China. E-mail: jlyang@ustc.edu.cn.*

Electronic supplementary information (ESI) available. See DOI: https://doi.org/xxx-xxx-xxx-xxx.

Content

HTC, (e) RhN_1O_3-HTC, (f) PdN_1O_3-HTC, (g) IrN_1O_3-HTC and (h) PtN_1O_3-HTC. The Fermi level is set at the zero of energy (dashed line in figures).

Fig. S9. Calculated partial density of states (PDOS) for the *p* orbitals of O/N atoms and *d* orbitals of TM atoms for (a) FeN_2O_2-HTC, (b) CoN_2O_2-HTC, (c) NiN_2O_2-HTC, (d) RuN_2O_2-HTC, (e) RhN_2O_2-HTC, (f) PdN_2O_2-HTC, (g) IrN_2O_2-HTC and (g) PtN_2O_2-HTC. The Fermi level is set at the zero of energy (dashed line in figures).

Fig. S10. Calculated partial density of states (PDOS) for the *p* orbitals of O/N atoms and *d* orbitals of TM atoms for (a) FeN_3O_1-HTC, (b) CoN_3O_1-HTC, (c) NiN_3O_1-HTC, (d) RuN_3O_1-HTC, (e) RhN_3O_1-HTC, (f) PdN_3O_1-HTC, (g) IrN_3O_1-HTC and (h) PtN_3O_1-HTC. The Fermi level is set at the zero of energy (dashed line in figures).

Fig. S11. Calculated charge transfer from TM atoms to N_xO_{4-x} substrates of TMN_xO_{4-x}-HTC obtained by Bader charge analysis. The positive value of Bader charge suggests that the charge is transferred from TM atoms to the substrates.

Fig. S12. (a) Calculated *d*-band center values for all the designed TMN_xO_{4-x}-HTC catalysts. Gibbs free energy of intermediates corresponding to the *d*-electron numbers of (b) TMN_4-HTC, (c) TMO_4-HTC, (d) TMN_1O_3-HTC, (e) TMN_2O_2-HTC, and (f) TMN_3O_1-HTC catalysts.

Fig. S13. Gibbs free energy of intermediates corresponding to the *d*-band center of (a) TMN_4-HTC, (b) TMO_4-HTC, (c) TMN_1O_3-HTC, (d) TMN_2O_2-HTC, and (e) TMN_3O_1-HTC catalysts.

Fig. S14. Calculated free energy diagrams of OER and ORR on (a) FeN_4-HTC, (b) CoN_4-HTC, (c) NiN_4-HTC, (d) RuN_4-HTC, (e) RhN_4-HTC, (f) PdN_4-HTC, (g) IrN_4-HTC and (h) PtN_4-HTC at zero potential. The yellow and pink values are the potential-determining step values for OER and ORR.

Fig. S15. Calculated free energy diagrams of OER and ORR on (a) FeO_4-HTC, (b) CoO_4-HTC, (c) NiO_4-HTC, (d) RuO_4-HTC, (e) RhO_4-HTC, (f) PdO_4-HTC, (g) IrO_4-HTC and (h) PtO_4-HTC at zero potential. The yellow and pink values are the potential-determining step values for OER and ORR.

Fig. S16. Calculated free energy diagrams of OER and ORR on (a) FeN_1O_3-HTC, (b) CoN_1O_3-HTC, (c) NiN_1O_3-HTC, (d) RuN_1O_3-HTC, (e) RhN_1O_3-HTC, (f) PdN_1O_3-HTC, (g) IrN_1O_3-HTC and (h) PtN_1O_3-HTC at zero potential. The yellow and pink values are the potential-determining step values for OER and ORR.

Fig. S17. Calculated free energy diagrams of OER and ORR on (a) FeN_2O_2-HTC, (b) CoN_2O_2-

HTC, (c) NiN_2O_2-HTC, (d) RuN_2O_2-HTC, (e) RhN_2O_2-HTC, (f) PdN_2O_2-HTC, (g) IrN_2O_2-HTC and (h) PtN_2O_2-HTC at zero potential. The yellow and pink values are the potential-determining step values for OER and ORR.

Fig. S18. Calculated free energy diagrams of OER and ORR on (a) FeN_3O_1-HTC, (b) CoN_3O_1-HTC, (c) NiN_3O_1-HTC, (d) RuN_3O_1-HTC, (e) RhN_3O_1-HTC, (f) PdN_3O_1-HTC, (g) IrN_3O_1-HTC and (g) PtN_3O_1-HTC at zero potential. The yellow and pink values are the potential-determining step values for OER and ORR.

Fig. S19. Total energy variations of (a) CoN_3O_1-HTC and (b) RhN_3O_1-HTC as the function of time for AIMD simulation under 500 K condition. The snapshot of atomic configurations at the end of the AIMD simulation are inserted.

Fig. S20. Total energy variations of (a) CoN_2O_2-HTC and (b) RhN_2O_2-HTC as the function of time for AIMD simulation under 500 K condition. The snapshot of atomic configurations at the end of the AIMD simulation are inserted.

Fig. S21. Total energy variations of (a) CoN_1O_3-HTC and (b) RhN_1O_3-HTC as the function of time for AIMD simulation under 500 K condition. The snapshot of atomic configurations at the end of the AIMD simulation are inserted.

Fig. S22. Total energy variations of (a) CoO_4-HTC and (b) RhO_4-HTC as the function of time for AIMD simulation under 500 K condition. The snapshot of atomic configurations at the end of the AIMD simulation are inserted.

Table S1. The detailed average bond length between TM and N/O atoms change after different TM doping.

Table S2. For comparison, the calculated overpotentials for the OER (η^{OER}) and ORR (η^{ORR}) on the 2D-MOF materials are listed. The unit for η is V.

1. OER and ORR

The overall OER process includes a four-stage pathway, which can be described as follows in the acidic environment:

$$2H_2O \rightarrow 4H^+ + O_2 + 4e- \quad (1)$$

The four electron reaction paths of OER are defined as equations (a) - (d) as reported in the previous literature [1]:

$$H_2O\ (l) + * \rightarrow HO* + H^+ + e- \quad (a)$$

$$HO* \rightarrow O* + H^+ + e- \quad (b)$$

$$O* + H_2O\ (l) \rightarrow HOO* + H^+ + e- \quad (c)$$

$$HOO* \rightarrow * + O_2\ (g) + H^+ + e- \quad (d)$$

Where * represents active sites on the catalyst, (*l*) and (g) is the liquid and gas phase, respectively, and O*, HO* and HOO* are the corresponding adsorbed intermediates. The Gibbs free energy (ΔG) of each elementary step under the U = 0 and pH = 0 condition was calculated by the following equations (1a~1d):

$$\triangle G_a = G_{HO*} + 1/2G_{H2,g} - G_{H2O,l} - G_* \quad (1a)$$

$$\triangle G_b = G_{O*} + 1/2G_{H2,g} - G_{HO*} \quad (1b)$$

$$\triangle G_c = G_{HOO*} + 1/2G_{H2,g} - G_{O*} - G_{H2O,l} \quad (1c)$$

$$\triangle G_d = \{4.92eV + 2G_{H2O,l} - 2G_{H2,g}\} + 1/2G_{H2,g} + G_* - G_{HOO*} \quad (1d)$$

Where we defined $G_{X*}=E_{X*}+ZPE_{X*}-TS_{X*}$, X refers to HO*, O* and HOO*. Here E_{X*} is the DFT total energy of the corresponding X* system under the polarization solvent model calculation. ZPE_{X*} refers to the zero-point energy of X*. Here we only include the zero-point energy of X*, while keeping the catalyst * fixed. TS_{X*} is the calculated entropy term of the adsorbed intermediate. Finally, $G_*=E_*$ is the total energy of catalyst under the DFT solvent model calculation. Due to the poor description of DFT for the high-spin ground state of the O_2, we used $G_{O2,g} + 4G_{H2,g} - 2G_{H2O,l} = 4.92$ eV to obtain the free energy of O_2 in the gas phase [2]. It is also difficult to directly calculate the Gibbs free energy of H_2O in the liquid phase ($G_{H2O,l}$). It is customary to calculate the liquid phase Gibbs free energy from its vapor phase counterpart at their equilibrium pressure when they have the same Gibbs free energies. Then, $G_{H2O,l} = E_{H2O} + ZPE_{H2O} - TS_{H2O}$. Where, E_{H2O} is total energy of H_2O in the gas phase obtained from the DFT calculation; ZPE_{H2O} is the zero point energy; TS_{H2O} is the entropy term of the gas phase (in equilibrium with the liquid phase). We took the values of 0.67 eV and 0.41 eV for the TS_{H2O}

and TS_{H2}, respectively [3]. The free energy changes for the above four OER processes can be described as $\Delta G_a = \Delta G_{HO*}$, $\Delta G_b = \Delta G_{O*} - \Delta G_{HO*}$, $\Delta G_c = \Delta G_{HOO*} - \Delta G_{O*}$, and $\Delta G_d = 4.92 - \Delta G_{HOO*}$. As the most important measure of the catalytic activities for OER, overpotential η of OER (η^{OER}) was calculated by equation (2):

$$\eta^{OER} = \frac{\max\{\Delta G_a,\ \Delta G_b,\ \Delta G_c,\ \Delta G_d\}}{e} - 1.23 \quad (2)$$

ORR, as a reverse reaction of the OER, its overpotential (η^{ORR}) can be calculated by the following equation (3):

$$\eta^{ORR} = 1.23 - \frac{\min\{\Delta G_a,\ \Delta G_b,\ \Delta G_c,\ \Delta G_d\}}{e} \quad (3)$$

2. The detailed crystal information for the calculation of chemical potential of metal atoms

The corresponding most stable bulk structure of Fe, Co, Ni, Ru, Rh, Pd, Ir and Pt is the body-centered cubic (BCC), hexagonal close-packed (HCP), faced-centered cubic (FCC), HCP, FCC, FCC, FCC and FCC, respectively.

3. The catalytic selectivity of the ORR

The rate constant *k* can be obtained based on the Arrhenius equation: $k = A \exp(-\Delta G_{PDS}/k_B T)$. Here, *A*, k_B and T refers to the pre-exponential factor, the Boltzmann constant and the temperature of 298.15 K, respectively. Hence, we can obtain the following equation: $\ln(k_{sys}/k_{Pt(111)}) = [\Delta G_{PDS}(Pt(111) - \Delta G_{PDS}(sys)]/k_B T$. Here, k_{sys} and $k_{Pt(111)}$ refer to the rate constant of the ORR on the screened electrocatalysts and ORR on the benchmark catalyst Pt(111), respectively. The selectivity of a certain catalyst can be estimated from the ratio of rate constants k_{O2} and k_{H2O2} as shown in the following equation: $\ln(k_{O2}/k_{H2O2}) = [\Delta G(H_2O_2 - \Delta G(O*)]/k_B T$. Here, k_{O2} and k_{H2O2} refers to the rate constant of O* formation from HOO* and H_2O_2 formation from HOO*, respectively.

4. The polarization curves simulation of OER and ORR

For a given electrochemical process O + *ne* ⇌ R under one electric potential *U*, it can be used the well-known Nernst equation to link the concentrations of the reactant and the product [4] by the following equation (4):

$$U = U_0 + \frac{RT}{nF} ln(\frac{C_O}{C_R}) \quad (4)$$

Here, U_0 refers to the equilibrium potential of the reaction at the standard state, *R* refers to the universal gas constant, *T* refers to the temperature, *n* refers to the electron transfer number, F refers to the Faraday constant, and C_O/C_R refers to the concentration of the reactant/product in this reaction [5]. Therefore, the exchange current density j_0 can be calculated by the following equation (5):

$$j_0 = nFkC_O \exp\left[-\frac{\alpha F}{RT}(U_{eq} - U_0)\right] = \mathrm{nFkC}_O^{1-\alpha}\mathrm{C}_R^{\alpha} \quad (5)$$

Where *k* refers to the reaction rate constant, U_{eq} refers to the equilibrium potential, and α refers to the transfer coefficient. So, the electrochemical polarization equation can be defined by equation (6):

$$j = j_0\left[\exp(-\frac{\alpha F}{RT}\eta) - \exp(\frac{(1-\alpha)F}{RT}\eta)\right] \quad (6)$$

Where $\eta = U - U_{eq}$ refers to the overpotential deviated from the equilibrium potential and *j* of the overall current density. The exchange current density j_0 can be used to evaluate the catalytic activity of one catalyst. Following the electrochemical catalysis mode developed by Nørskov *et al*., [1] the reaction rate constant *k* can be defined as follows:

$$k = k_0 exp\left[-\frac{\Delta G_{max}}{k_b T}\right] \quad (7)$$

Where k_b and ΔG_{max} refers to the Boltzmann constant and the Gibbs free energy change of the potential-determining step, respectively. In the electrochemical polarization model [6], k_0 is defined as the equation (8):

$$k_0 = \frac{k_b T}{h} \quad (8)$$

Where *h* refers to the Planck constant. Therefore, the exchange current density j_0 of the electrochemical reaction when the reaction approaches its equilibrium state can be described as the following equation (9):

$$j_0 = \mathrm{nFC}_O \frac{k_b T}{h} \exp\left[- \frac{\Delta G_{max}}{k_b T} \right] \quad (9)$$

Hence, the overall current density j can be calculated by the follows equation (10) according to the overpotential η [6]:

$$j = \mathrm{nFC}_O \frac{k_b T}{h} \exp\left[- \frac{\Delta G_{max}}{k_b T} \right] \left[\exp(- \frac{\alpha F}{RT} \eta) - \exp(\frac{(1-\alpha) F}{RT} \eta) \right] \approx \mathrm{nFC}_O \frac{k_b T}{h} \exp\left[- \frac{\Delta G_{max}}{k_b T} - \frac{\alpha F}{RT} \eta \right] \quad (10)$$

The OER and ORR need to overcome the reaction kinetic energy barriers, and the onset potential generally represents the reaction potential at which the current begins to deviate from the baseline [7]. In this work, the calculated polarization curves for the OER and ORR was calculated as literature reported [8]. In detail, the potential U that prompts the OER and ORR catalytic process to proceed spontaneously was defined as the lowest potential. As known, U_{OER} is usually higher and U_{ORR} is lower than the standard O_2/H_2O potential of 1.23 V versus RHE at 298 K. The overpotential using the standard reaction potential is used to indicate the strength of the catalytic effect. Therefore, based on the equation 10, the j_{OER} and j_{ORR} values can be obtained from the following equations 11 and 12, respectively:

$$j_{OER} = \mathrm{nFC}_O \frac{k_b T}{h} \exp\left[- \frac{\Delta G_{max}}{k_b T} - \frac{\alpha F}{RT} (U_{OER} - 1.23) \right] (U_{OER} \geq 1.23) \quad (11)$$

$$j_{ORR} = \mathrm{nFC}_O \frac{k_b T}{h} \exp\left[- \frac{\Delta G_{max}}{k_b T} - \frac{\alpha F}{RT} (1.23 - U_{ORR}) \right] (0 \leq U_{ORR} \leq 1.23) \quad (12)$$

The expression corresponding to each curve is derived from the following equation 11. The change in Gibbs free energy for the potential-determining step (ΔG_{max}) can be directly obtained from the calculated free energy diagrams of the OER and ORR. Thus, based on the equations 11 and 12, the change in current density as a function of potential can be obtained from the following equation 13:

$$j(U) = \begin{cases} nF C_O \frac{k_b T}{h} exp\left[- \frac{\Delta G_{max}^{OER}}{k_b T} - \frac{\alpha F}{RT} (U_{OER} - 1.23) \right], & U_{OER} \geq 1.23 \\ nF C_O \frac{k_b T}{h} exp\left[- \frac{\Delta G_{max}^{ORR}}{k_b T} - \frac{\alpha F}{RT} (1.23 - U_{ORR}) \right], & 0 \leq U_{ORR} \leq 1.23 \end{cases} \quad (13)$$

Moreover, in this work, as above defined, the C_O and α refers to the concentration of the eactant/product in this reaction and the transfer coefficient, respectively. The values of C_O and α that reference previous literature [8] are taken as 1.0 x 10^{-3} *m*M and 0.5, respectively.

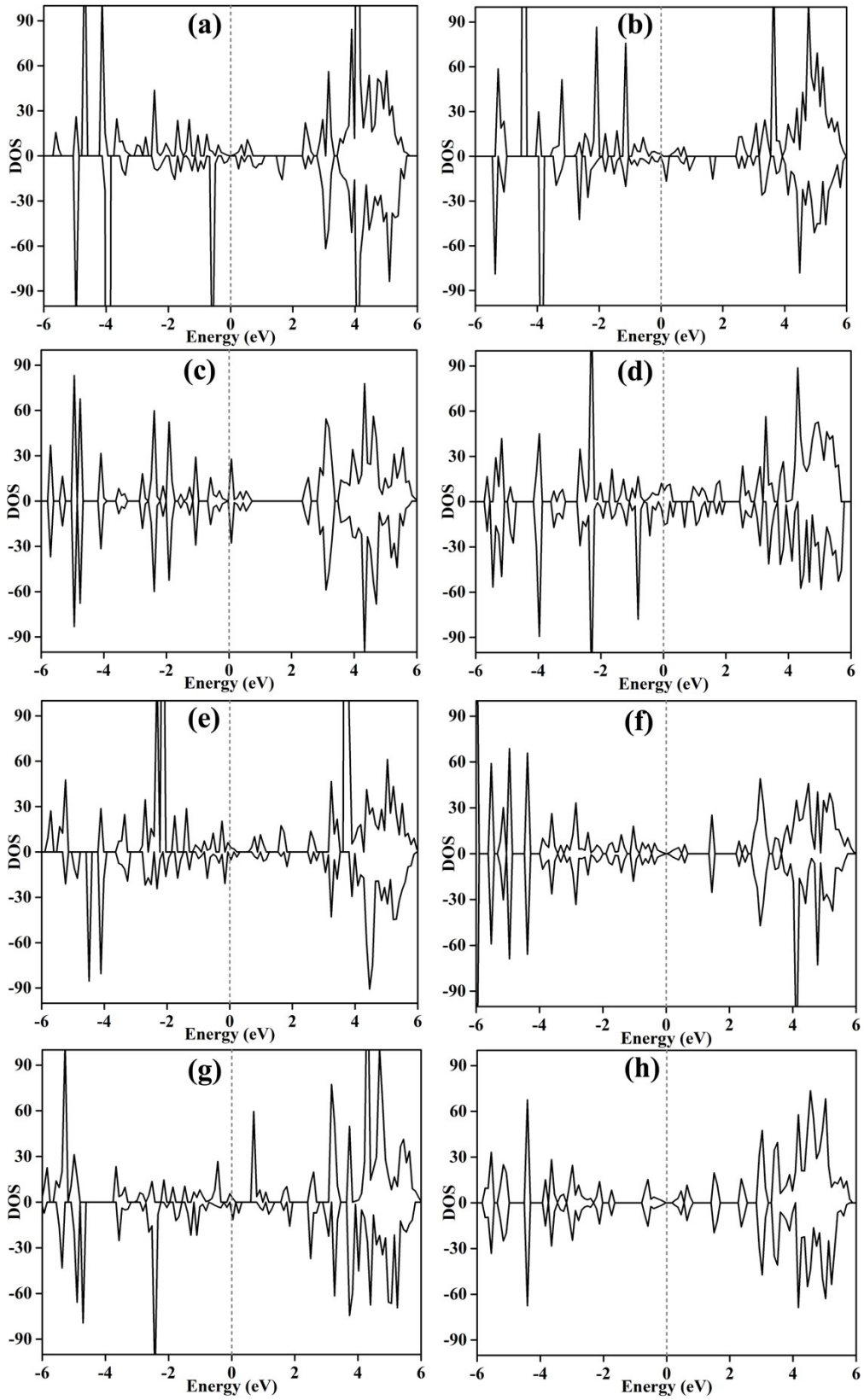

Fig. S1. Calculated density of states (DOS) for (a) FeN_4-HTC, (b) CoN_4-HTC, (c) NiN_4-HTC, (d) RuN_4-HTC, (e) RhN_4-HTC, (f) PdN_4-HTC, (g) IrN_4-HTC and (h) PtN_4-HTC. The Fermi level is set at the zero of energy (dashed line in figures).

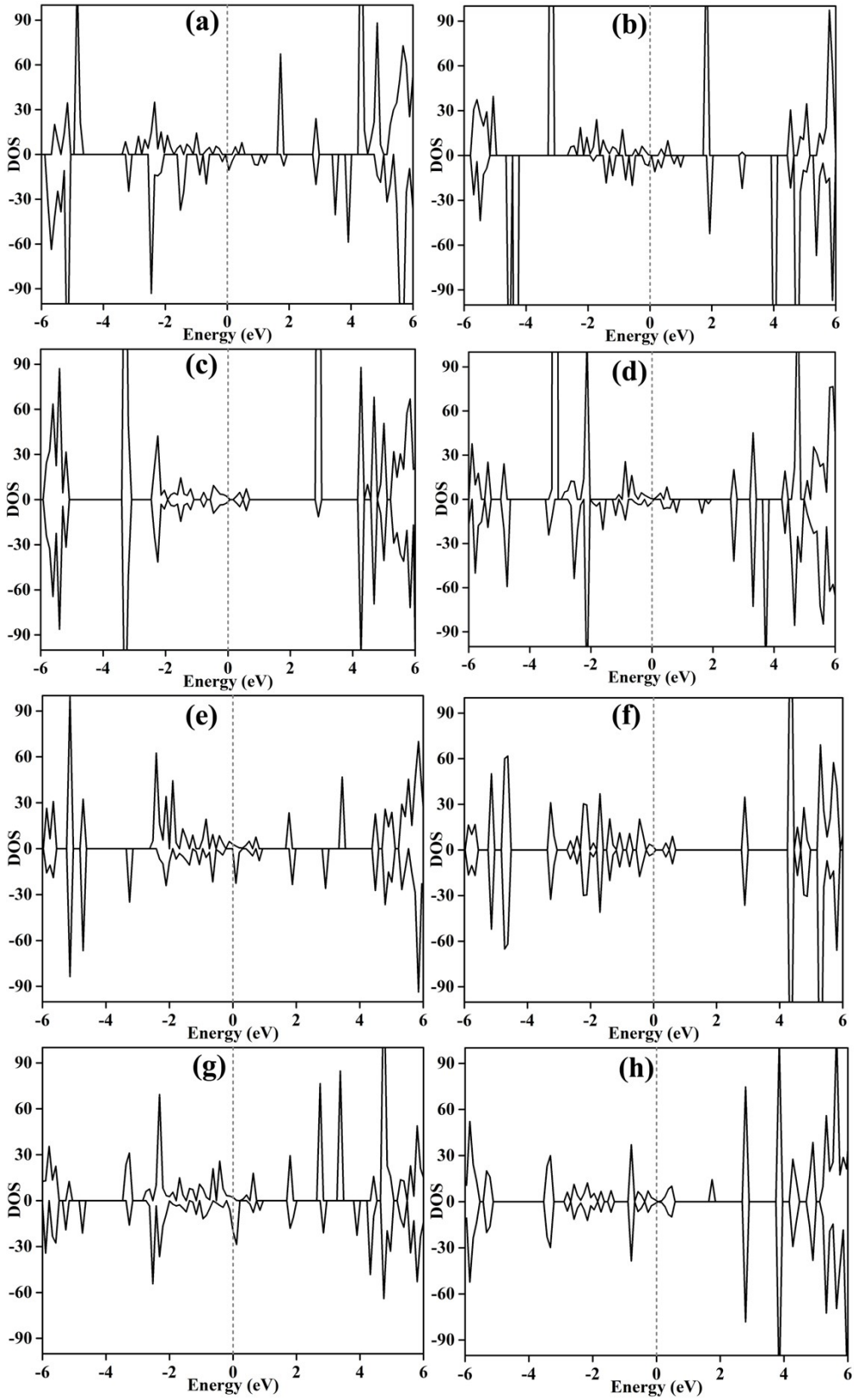

Fig. S2. Calculated density of states (DOS) for (a) FeO_4-HTC, (b) CoO_4-HTC, (c) NiO_4-HTC, (d) RuO_4-HTC, (e) RhO_4-HTC, (f) PdO_4-HTC, (g) IrO_4-HTC and (h) PtO_4-HTC. The Fermi level is set at the zero of energy (dashed line in figures).

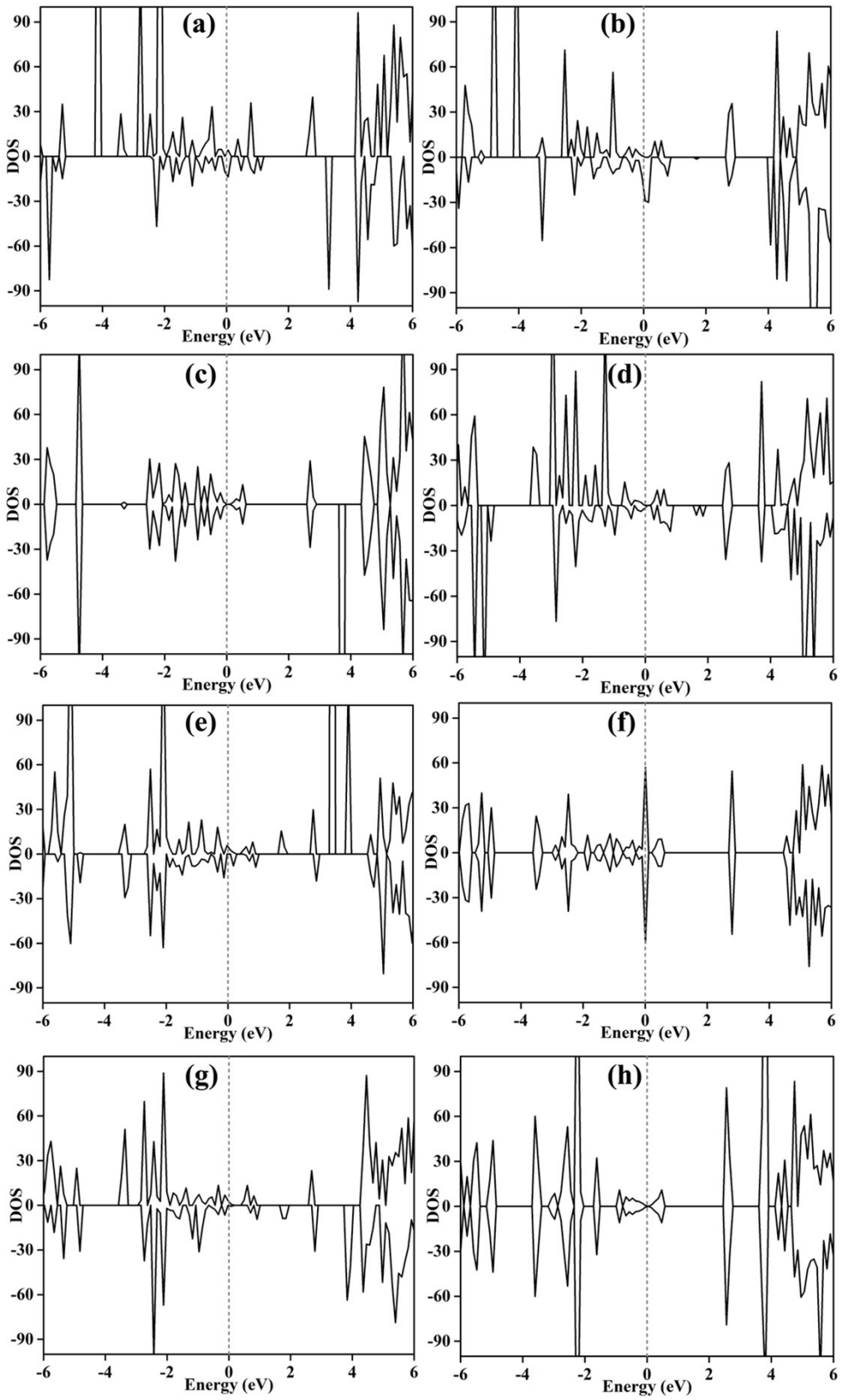

Fig. S3. Calculated density of states (DOS) for (a) FeN_1O_3-HTC, (b) CoN_1O_3-HTC, (c) NiN_1O_3-HTC, (d) RuN_1O_3-HTC, (e) RhN_1O_3-HTC, (f) PdN_1O_3-HTC, (g) IrN_1O_3-HTC and (h) PtN_1O_3-HTC. The Fermi level is set at the zero of energy (dashed line in figures).

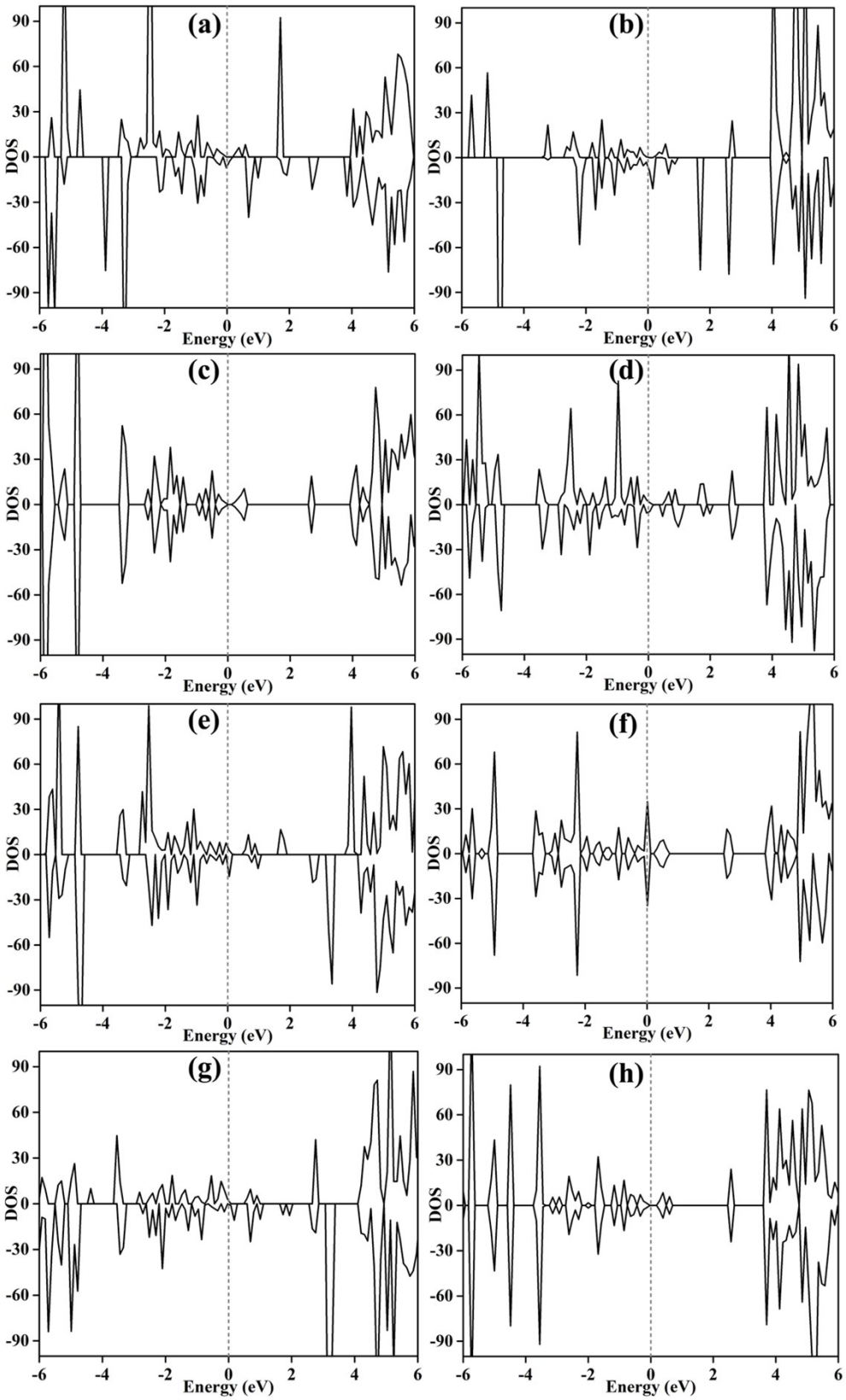

Fig. S4. Calculated density of states (DOS) for (a) FeN_2O_2-HTC, (b) CoN_2O_2-HTC, (c) NiN_2O_2-HTC, (d) RuN_2O_2-HTC, (e) RhN_2O_2-HTC, (f) PdN_2O_2-HTC, (g) IrN_2O_2-HTC and (h) PtN_2O_2-HTC. The Fermi level is set at the zero of energy (dashed line in figures).

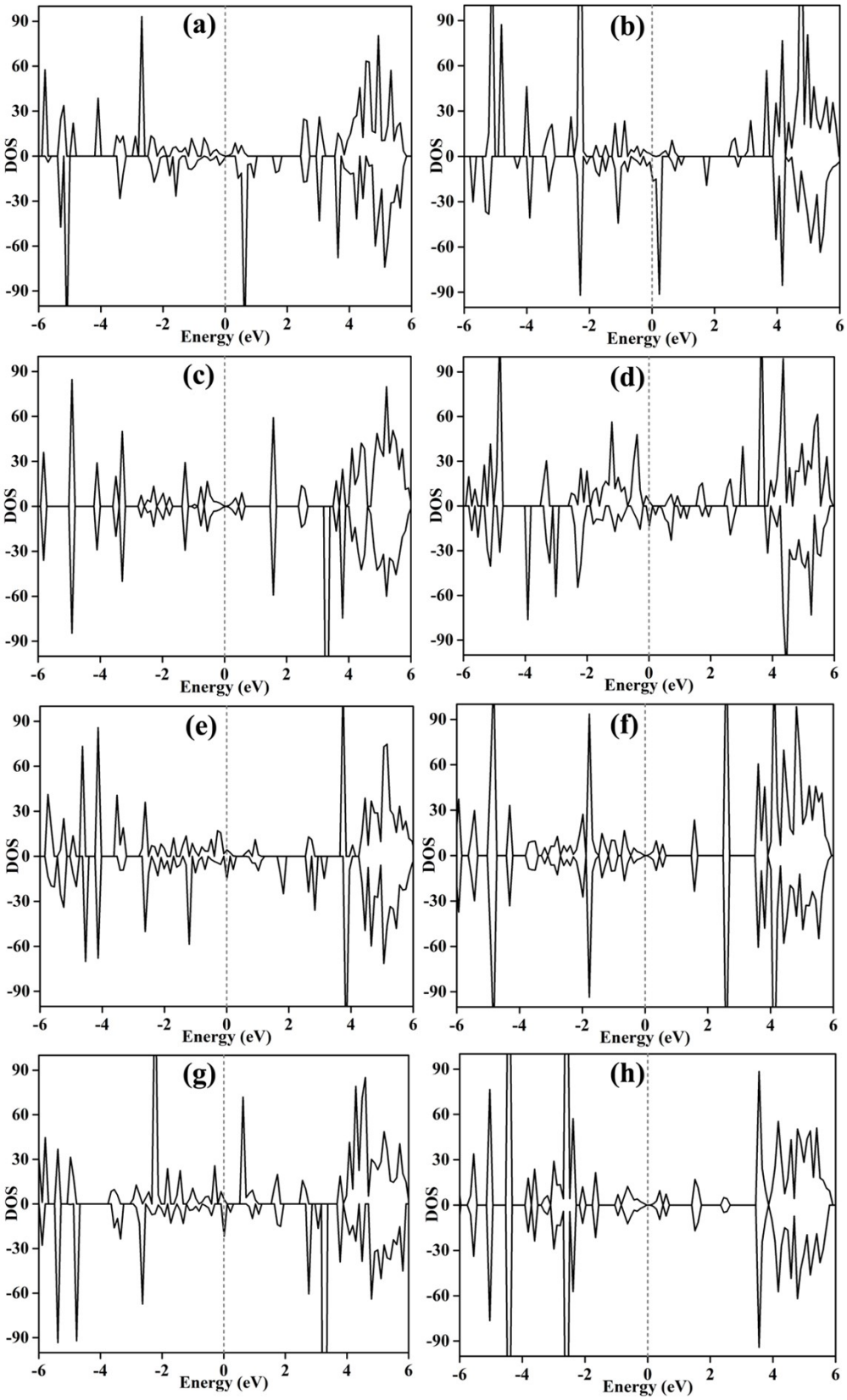

Fig. S5. Calculated density of states (DOS) for (a) FeN_3O_1-HTC, (b) CoN_3O_1-HTC, (c) NiN_3O_1-HTC, (d) RuN_3O_1-HTC, (e) RhN_3O_1-HTC, (f) PdN_3O_1-HTC, (g) IrN_3O_1-HTC and (h) PtN_3O_1-HTC. The Fermi level is set at the zero of energy (dashed line in figures).

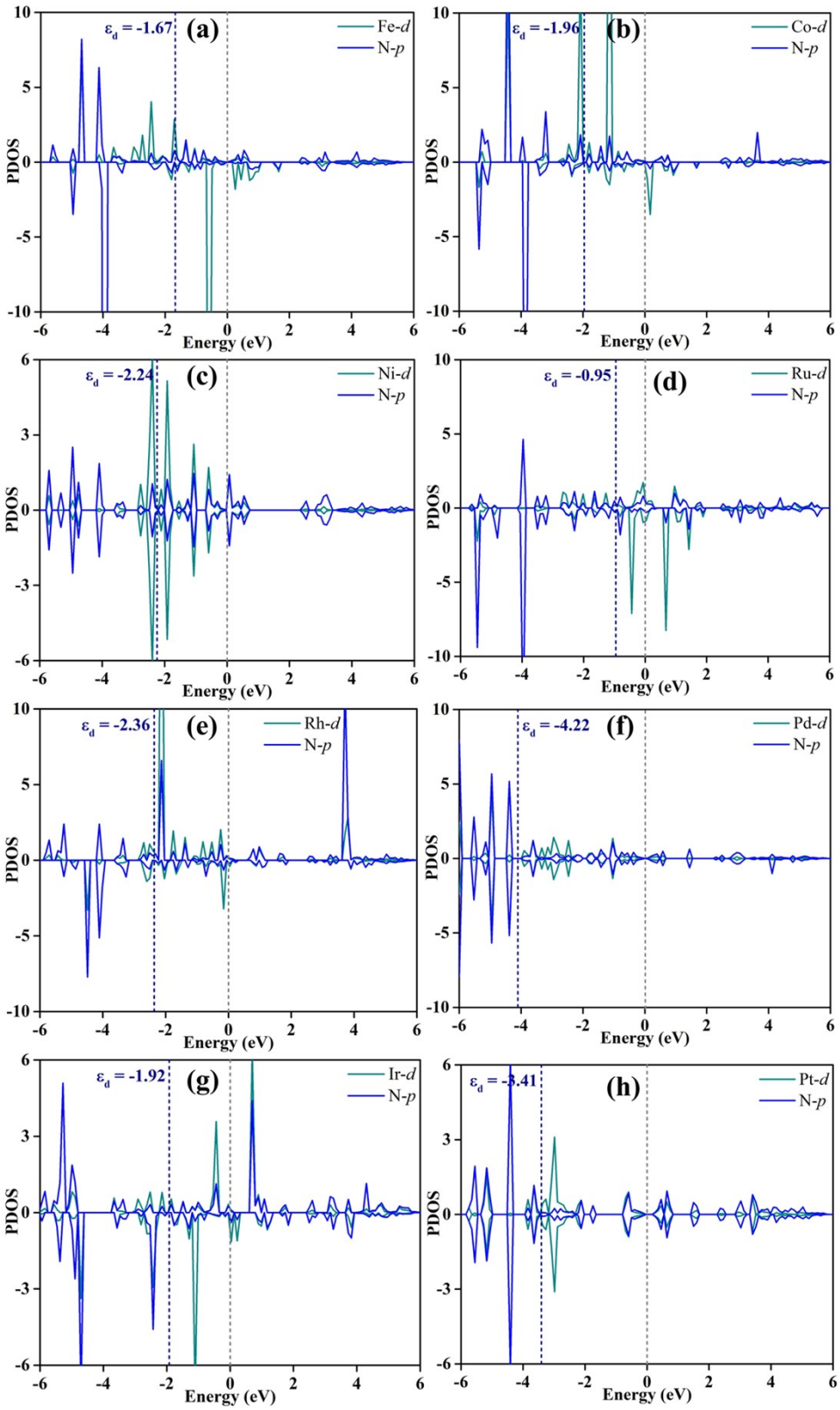

Fig. S6. Calculated partial density of states (PDOS) for the *p* orbitals of N atoms and *d* orbitals of TM atoms for (a) FeN_4-HTC, (b) CoN_4-HTC, (c) NiN_4-HTC, (d) RuN_4-HTC, (e) RhN_4-HTC, (f) PdN_4-HTC, (g) IrN_4-HTC and (h) PtN_4-HTC. The Fermi level is set at the zero of energy (dashed line in figures).

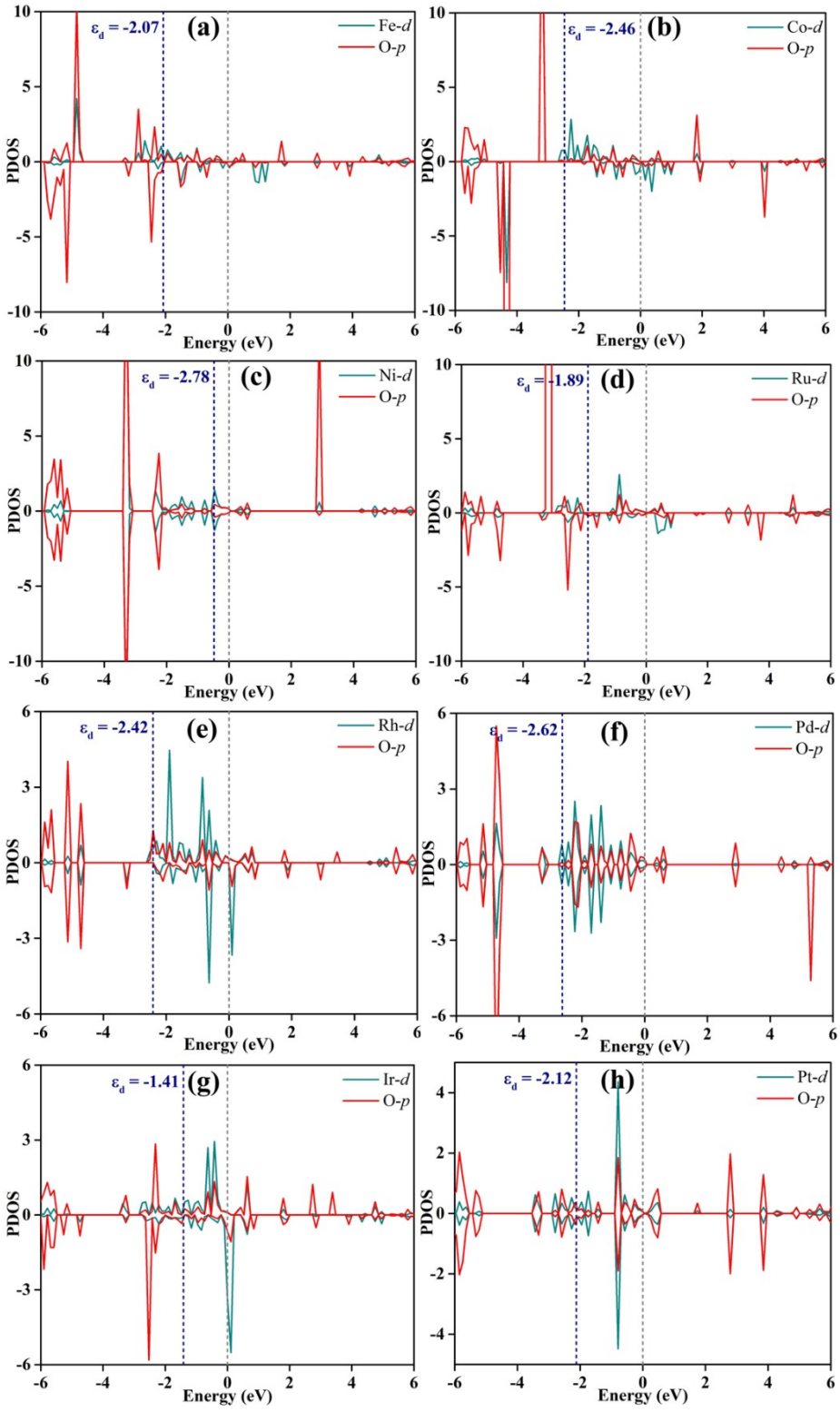

Fig. S7. Calculated partial density of states (PDOS) for the *p* orbitals of O atoms and *d* orbitals of TM atoms for (a) FeO_4-HTC, (b) CoO_4-HTC, (c) NiO_4-HTC, (d) RuO_4-HTC, (e) RhO_4-HTC, (f) PdO_4-HTC, (g) IrO_4-HTC and (h) PtO_4-HTC. The Fermi level is set at the zero of energy (dashed line in figures).

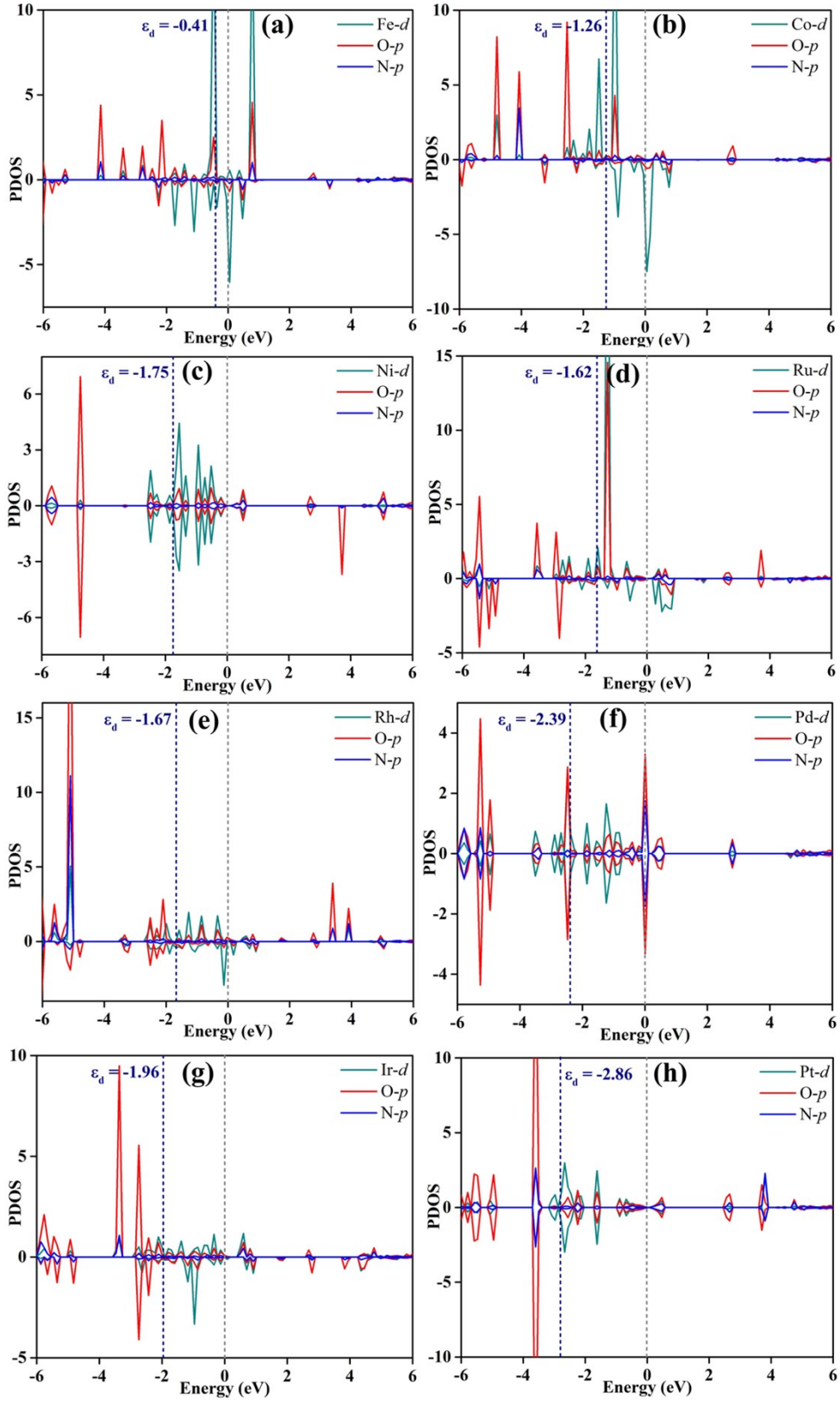

Fig. S8. Calculated partial density of states (PDOS) for the *p* orbitals of O/N atoms and *d* orbitals of TM atoms for (a) FeN_1O_3-HTC, (b) CoN_1O_3-HTC, (c) NiN_1O_3-HTC, (d) RuN_1O_3-HTC, (e) RhN_1O_3-HTC, (f) PdN_1O_3-HTC, (g) IrN_1O_3-HTC and (h) PtN_1O_3-HTC. The Fermi level is set at the zero of energy (dashed line in figures).

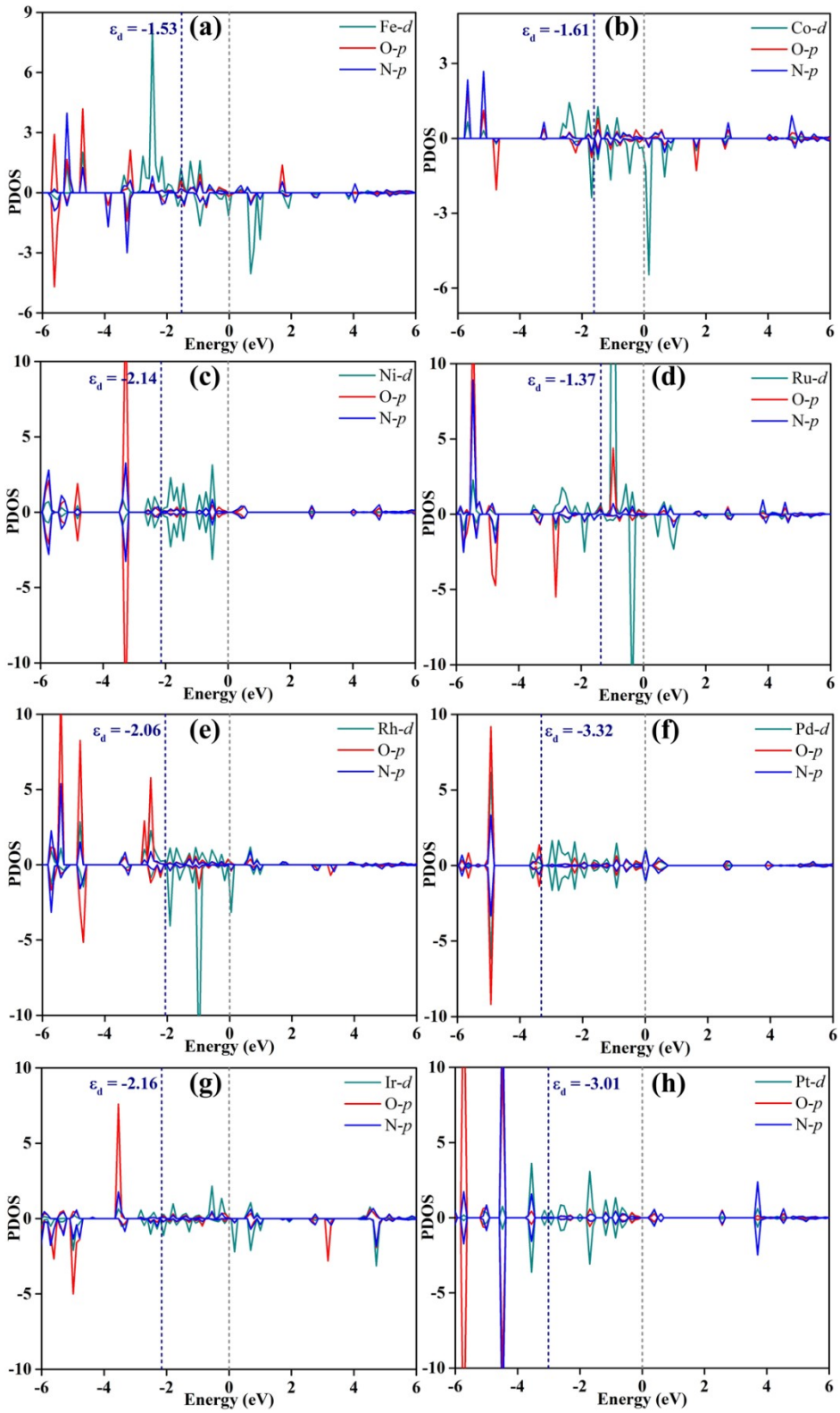

Fig. S9. Calculated partial density of states (PDOS) for the *p* orbitals of O/N atoms and *d* orbitals of TM atoms for (a) FeN_2O_2-HTC, (b) CoN_2O_2-HTC, (c) NiN_2O_2-HTC, (d) RuN_2O_2-HTC, (e) RhN_2O_2-HTC, (f) PdN_2O_2-HTC, (g) IrN_2O_2-HTC and (g) PtN_2O_2-HTC. The Fermi level is set at the zero of energy (dashed line in figures).

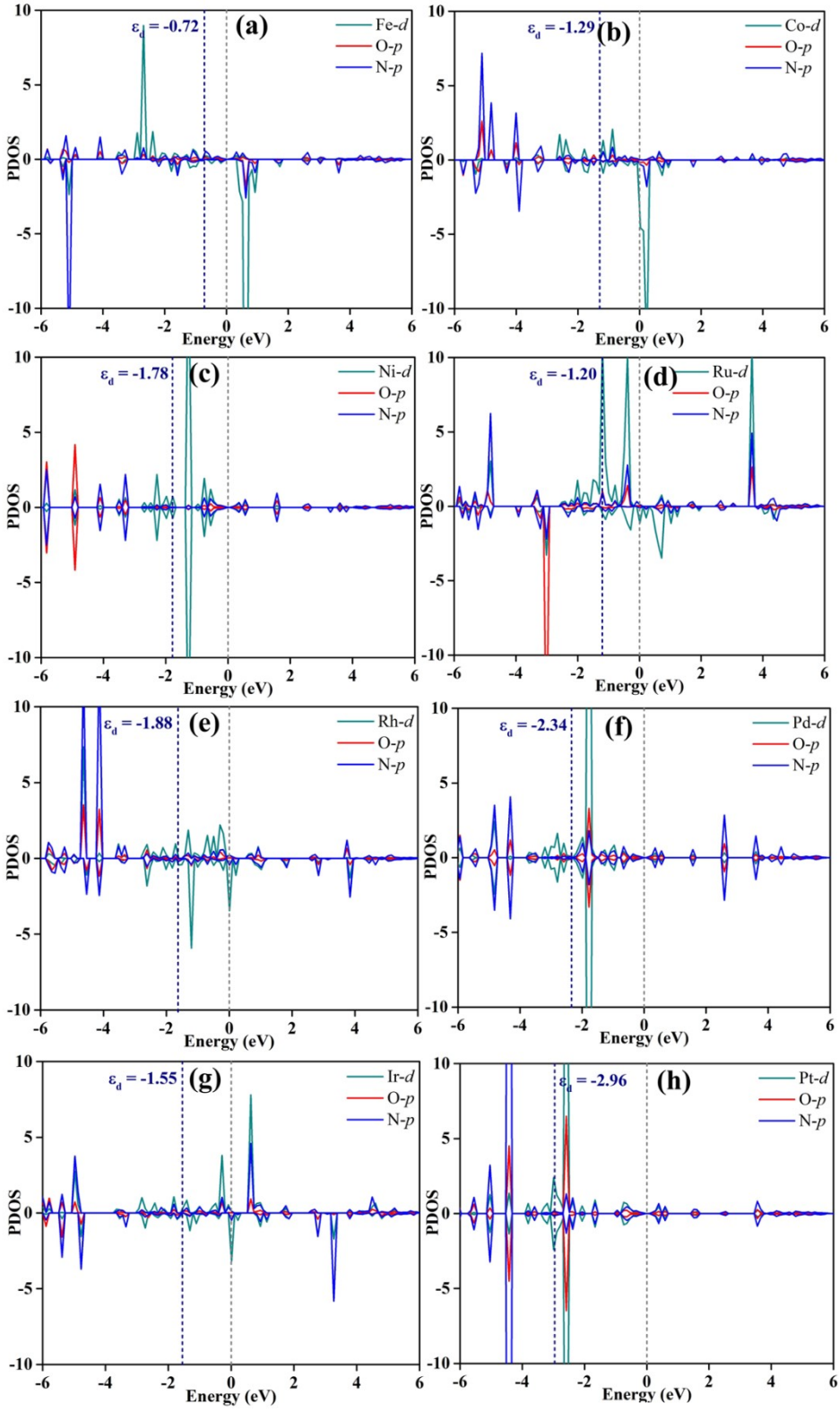

Fig. S10. Calculated partial density of states (PDOS) for the *p* orbitals of O/N atoms and *d* orbitals of TM atoms for (a) FeN_3O_1-HTC, (b) CoN_3O_1-HTC, (c) NiN_3O_1-HTC, (d) RuN_3O_1-HTC, (e) RhN_3O_1-HTC, (f) PdN_3O_1-HTC, (g) IrN_3O_1-HTC and (h) PtN_3O_1-HTC. The Fermi level is set at the zero of energy (dashed line in figures).

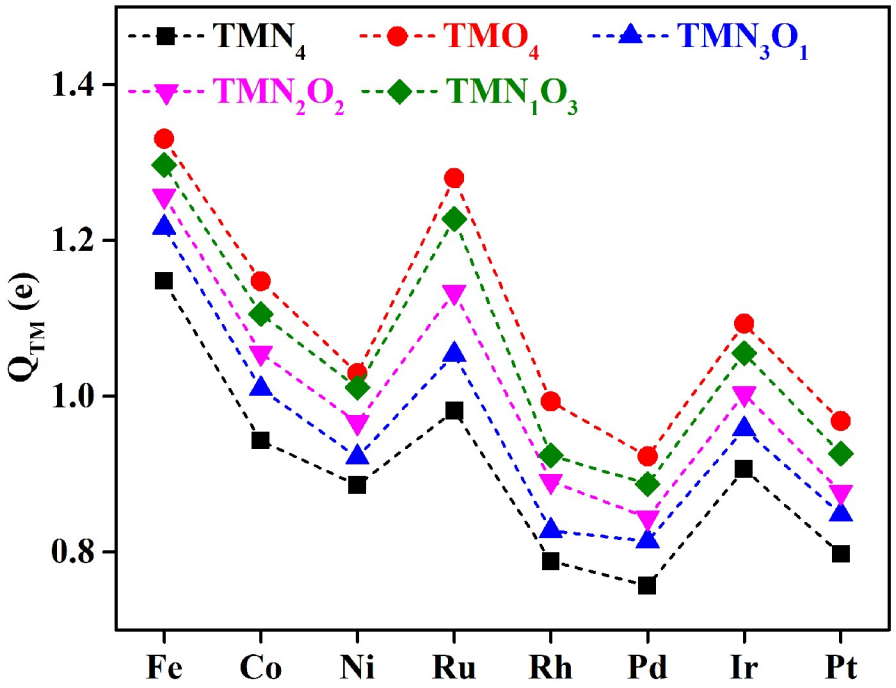

Fig. S11. Calculated charge transfer from TM atoms to N_xO_{4-x} substrates of TMN_xO_{4-x}-HTC obtained by Bader charge analysis. The positive value of Bader charge suggests that the charge is transferred from TM atoms to the substrates.

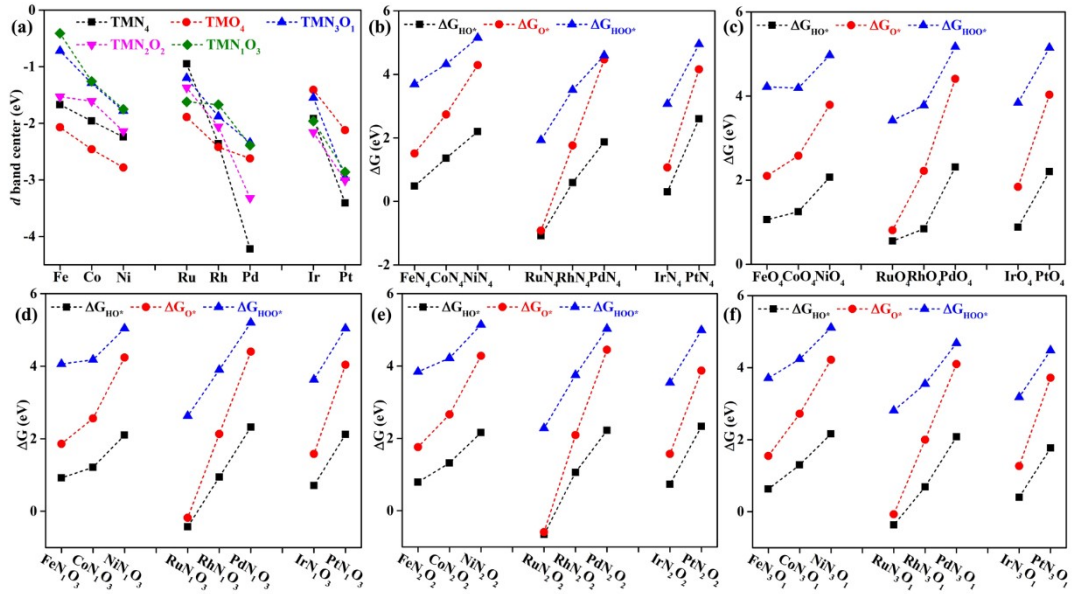

Fig. S12. (a) Calculated *d*-band center values for all the designed TMN_xO_{4-x}-HTC catalysts. Gibbs free energy of intermediates corresponding to the *d*-electron numbers of (b) TMN_4-HTC, (c) TMO_4-HTC, (d) TMN_1O_3-HTC, (e) TMN_2O_2-HTC, and (f) TMN_3O_1-HTC catalysts.

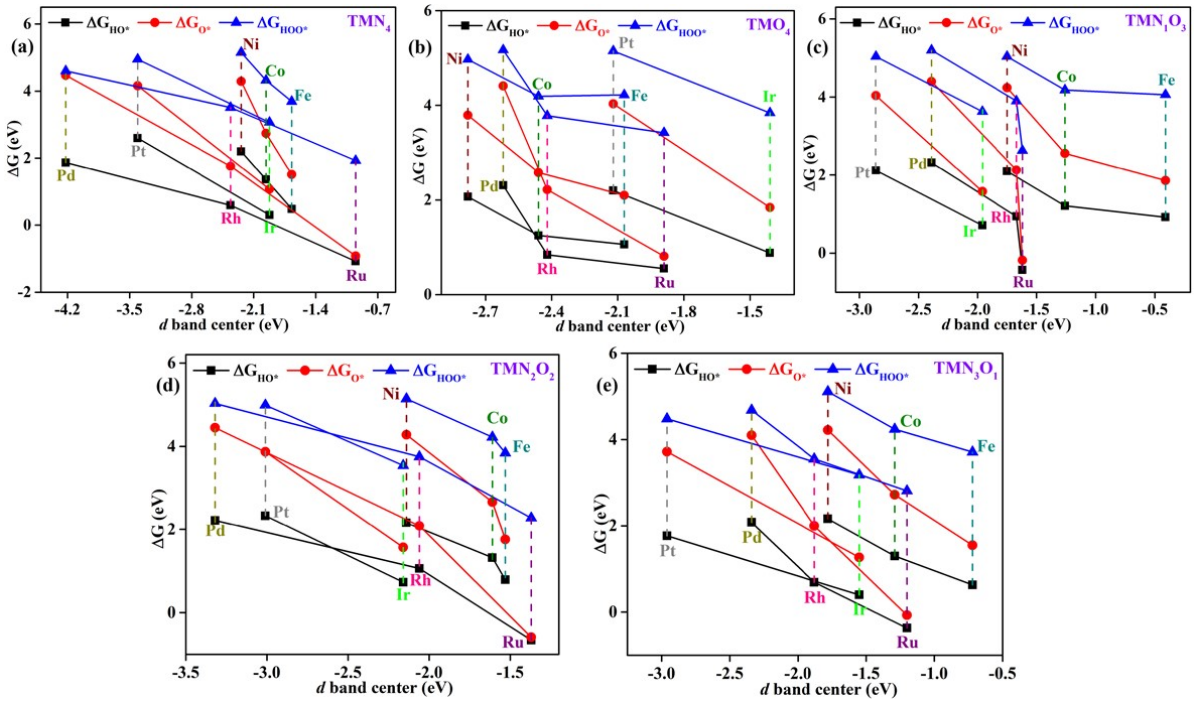

Fig. S13. Gibbs free energy of intermediates corresponding to the *d*-band center of (a) TMN_4-HTC, (b) TMO_4-HTC, (c) TMN_1O_3-HTC, (d) TMN_2O_2-HTC, and (e) TMN_3O_1-HTC catalysts.

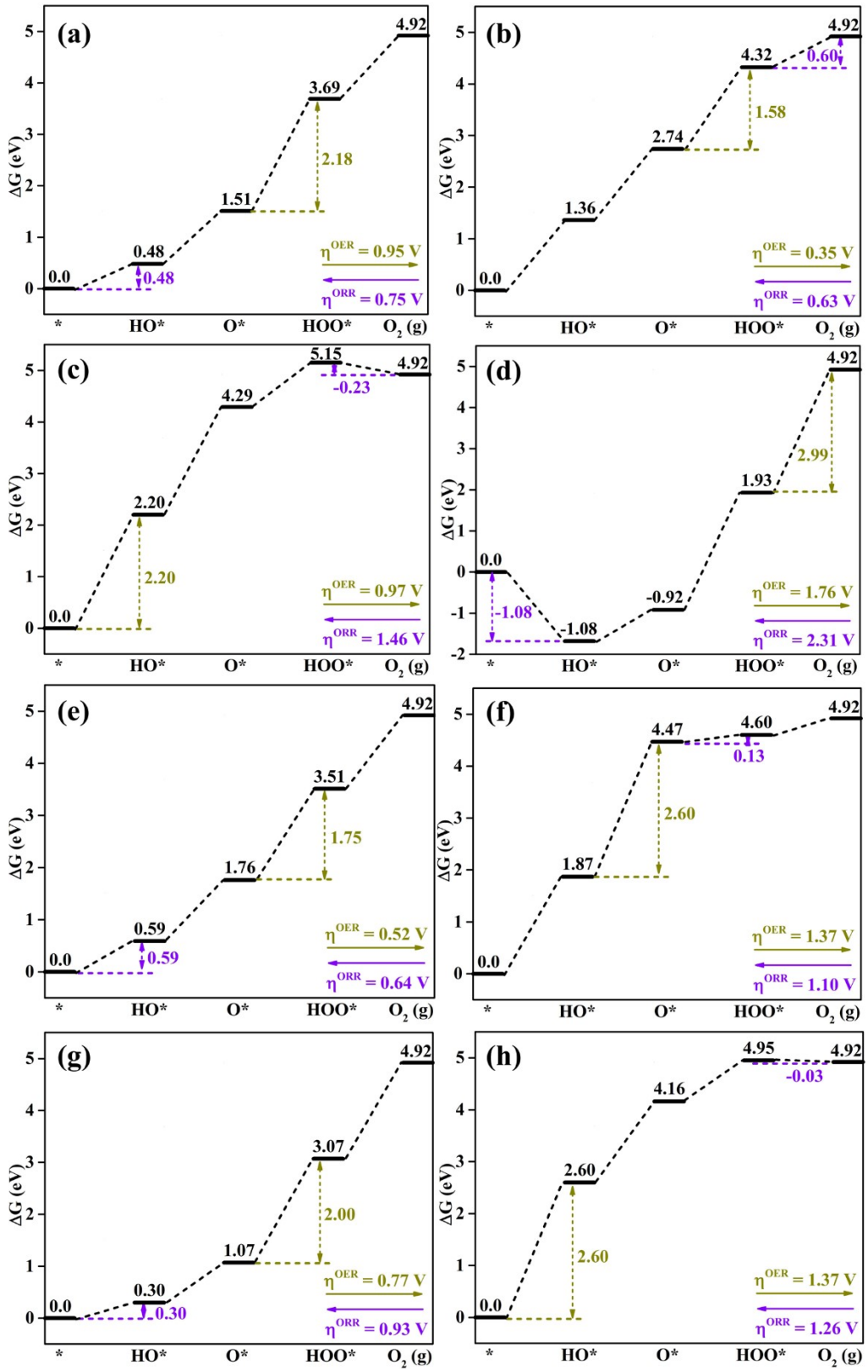

Fig. S14. Calculated free energy diagrams of OER and ORR on (a) FeN_4-HTC, (b) CoN_4-HTC, (c) NiN_4-HTC, (d) RuN_4-HTC, (e) RhN_4-HTC, (f) PdN_4-HTC, (g) IrN_4-HTC and (h) PtN_4-HTC at zero potential. The yellow and pink values are the potential-determining step values for OER and ORR.

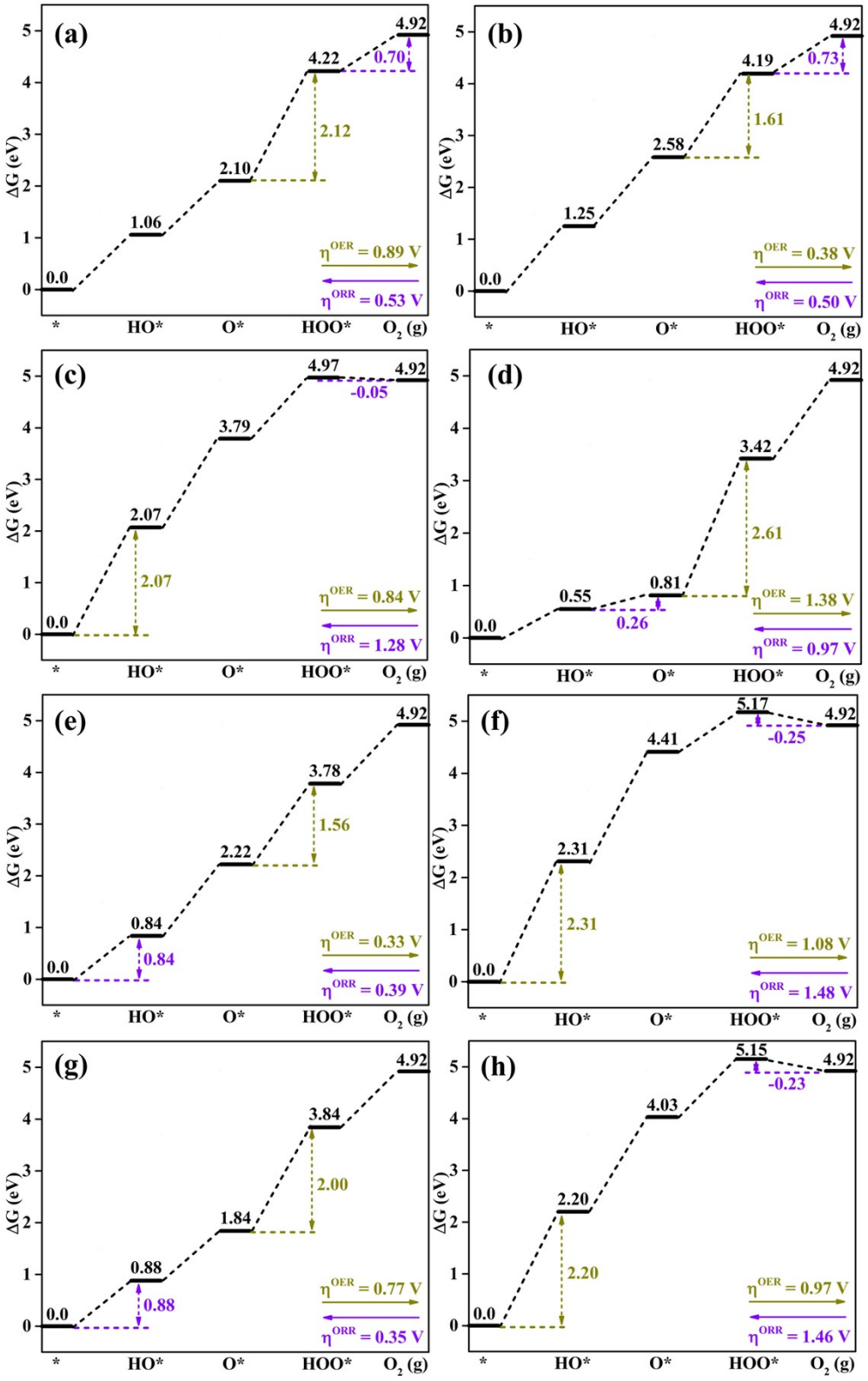

Fig. S15. Calculated free energy diagrams of OER and ORR on (a) FeO_4-HTC, (b) CoO_4-HTC, (c) NiO_4-HTC, (d) RuO_4-HTC, (e) RhO_4-HTC, (f) PdO_4-HTC, (g) IrO_4-HTC and (h) PtO_4-HTC at zero potential. The yellow and pink values are the potential-determining step values for OER and ORR.

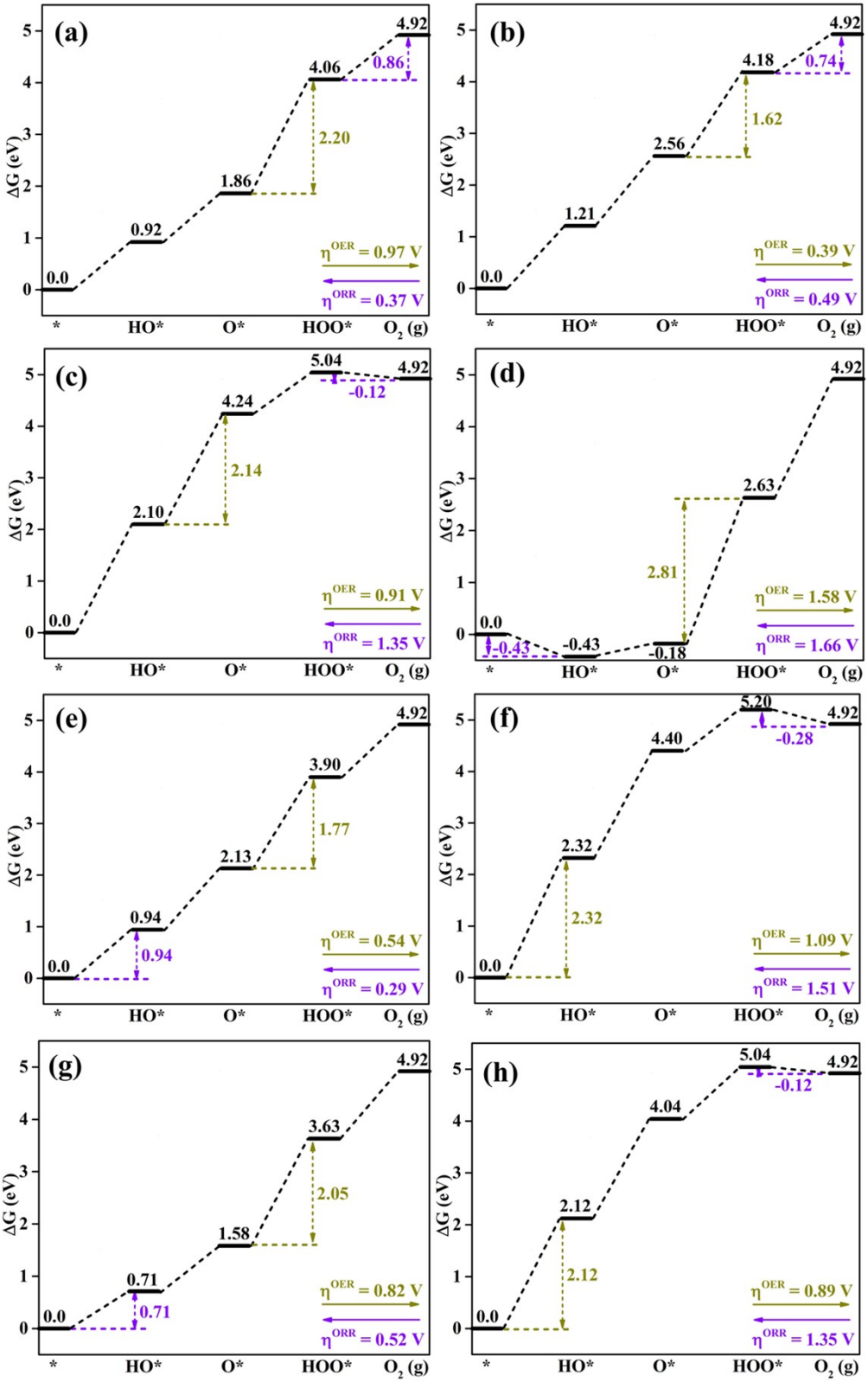

Fig. S16. Calculated free energy diagrams of OER and ORR on (a) FeN_1O_3-HTC, (b) CoN_1O_3-HTC, (c) NiN_1O_3-HTC, (d) RuN_1O_3-HTC, (e) RhN_1O_3-HTC, (f) PdN_1O_3-HTC, (g) IrN_1O_3-HTC and (h) PtN_1O_3-HTC at zero potential. The yellow and pink values are the potential-determining step values for OER and ORR.

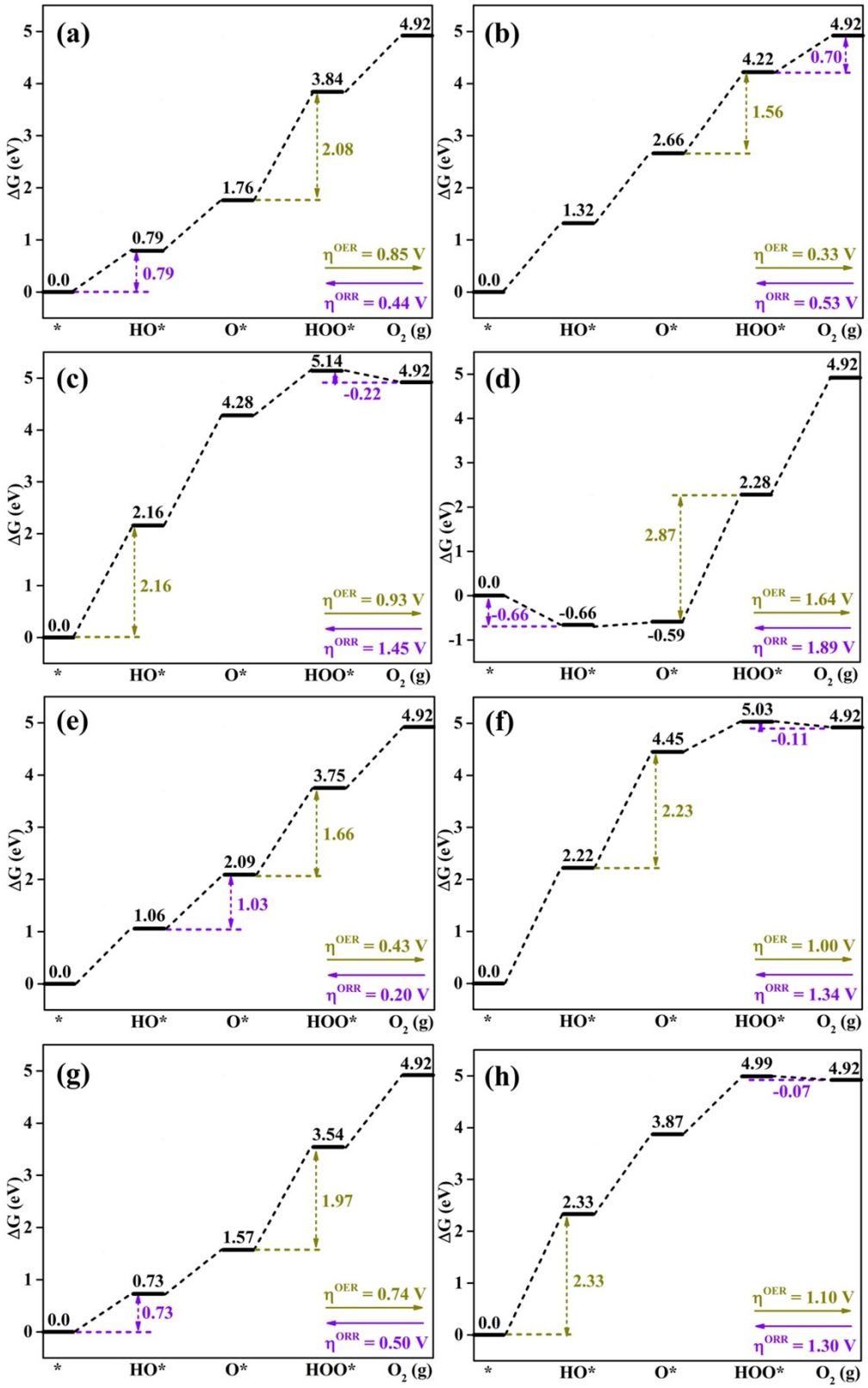

Fig. S17. Calculated free energy diagrams of OER and ORR on (a) FeN_2O_2-HTC, (b) CoN_2O_2-HTC, (c) NiN_2O_2-HTC, (d) RuN_2O_2-HTC, (e) RhN_2O_2-HTC, (f) PdN_2O_2-HTC, (g) IrN_2O_2-HTC and (h) PtN_2O_2-HTC at zero potential. The yellow and pink values are the potential-determining step values for OER and ORR.

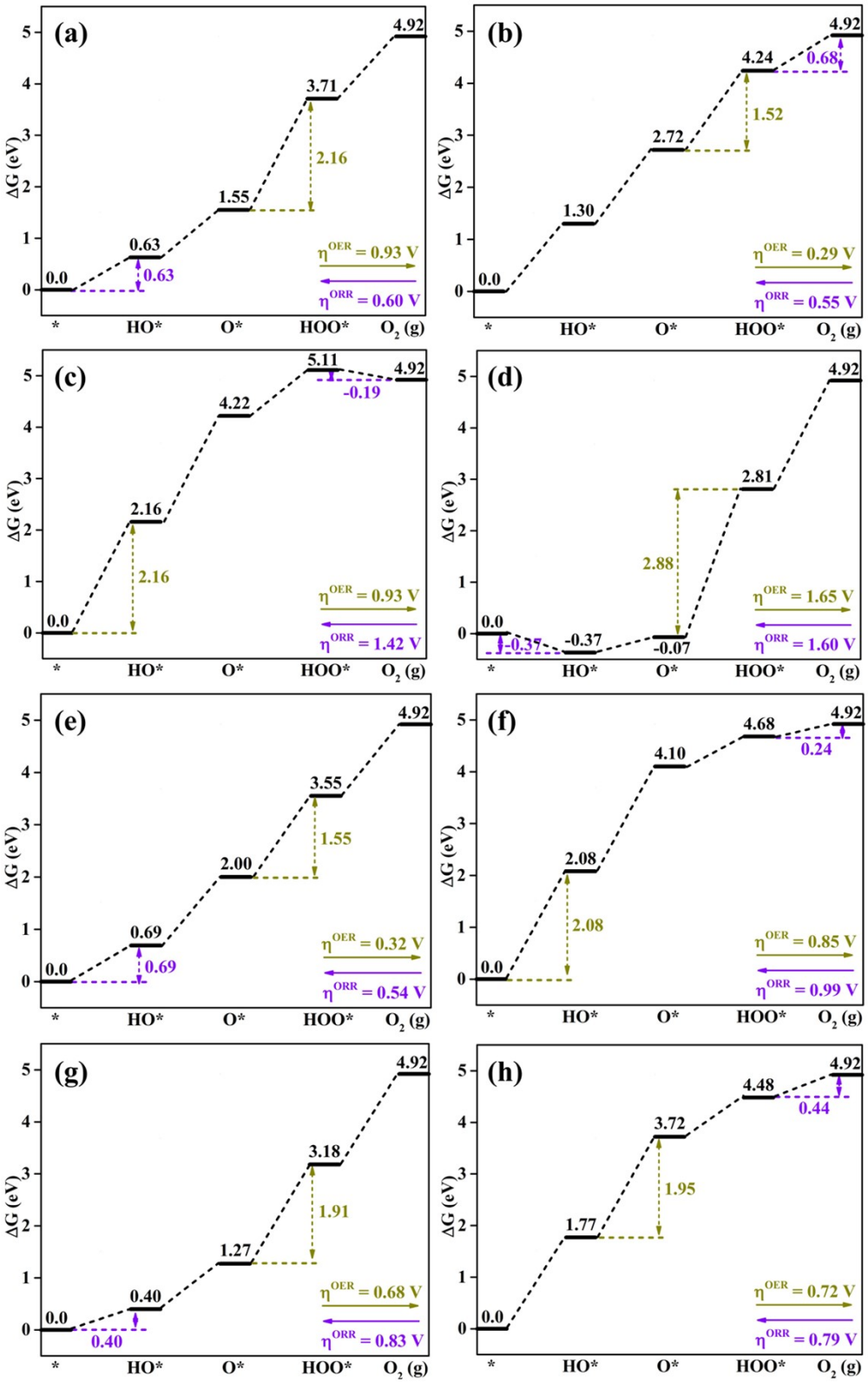

Fig. S18. Calculated free energy diagrams of OER and ORR on (a) FeN_3O_1-HTC, (b) CoN_3O_1-HTC, (c) NiN_3O_1-HTC, (d) RuN_3O_1-HTC, (e) RhN_3O_1-HTC, (f) PdN_3O_1-HTC, (g) IrN_3O_1-HTC and (g) PtN_3O_1-HTC at zero potential. The yellow and pink values are the potential-determining step values for OER and ORR.

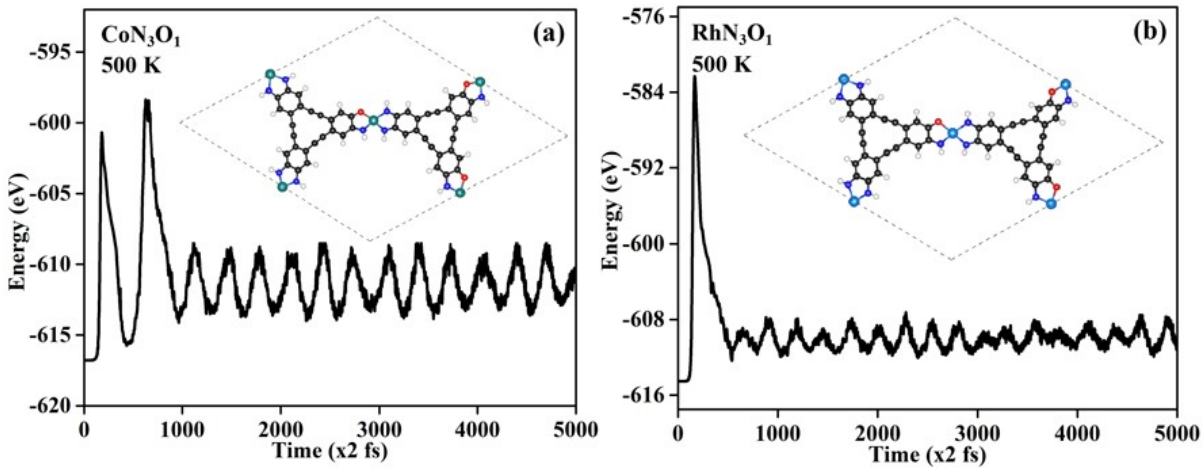

Fig. S19. Total energy variations of (a) CoN_3O_1-HTC and (b) RhN_3O_1-HTC as the function of time for AIMD simulation under 500 K condition. The snapshot of atomic configurations at the end of the AIMD simulation are inserted.

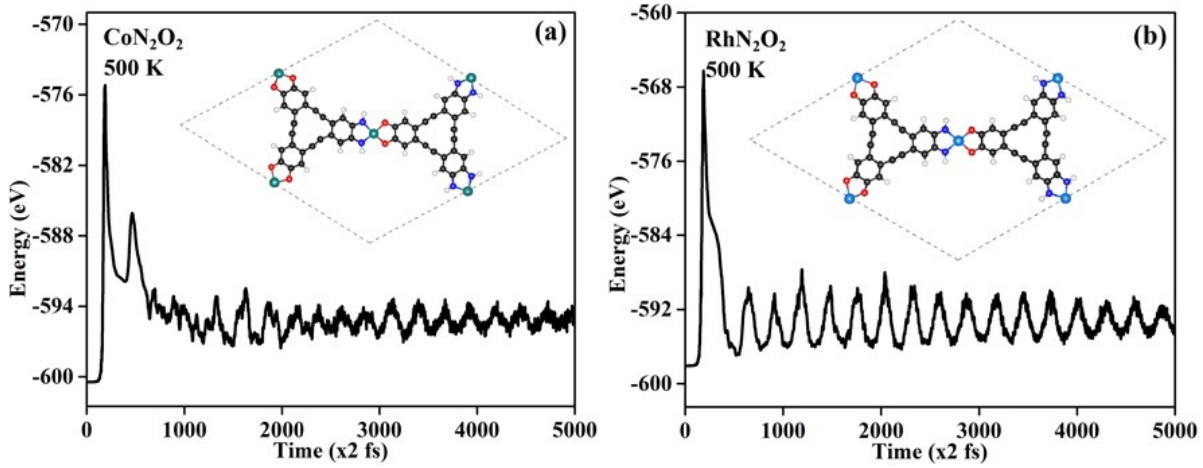

Fig. S20. Total energy variations of (a) CoN_2O_2-HTC and (b) RhN_2O_2-HTC as the function of time for AIMD simulation under 500 K condition. The snapshot of atomic configurations at the end of the AIMD simulation are inserted.

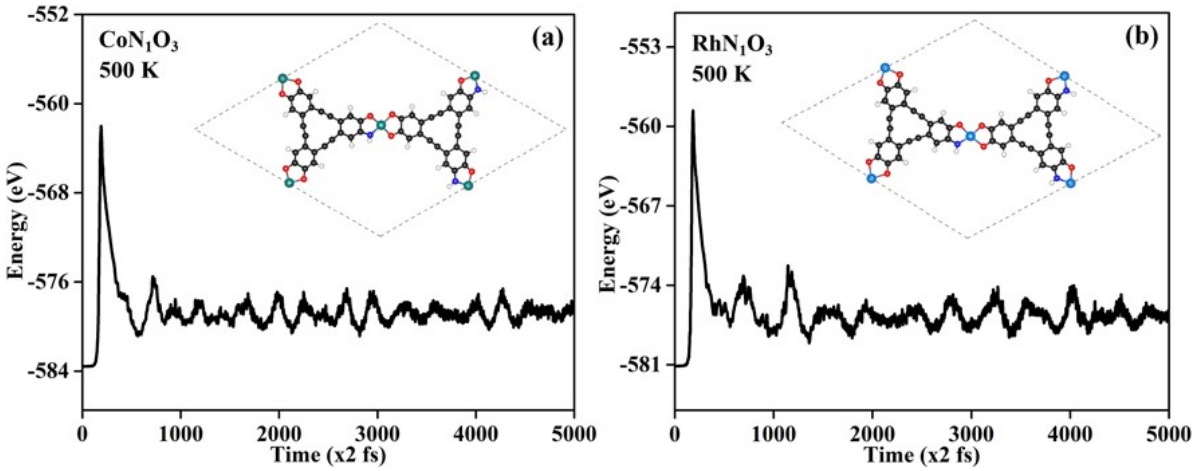

Fig. S21. Total energy variations of (a) CoN_1O_3-HTC and (b) RhN_1O_3-HTC as the function of time for AIMD simulation under 500 K condition. The snapshot of atomic configurations at the end of the AIMD simulation are inserted.

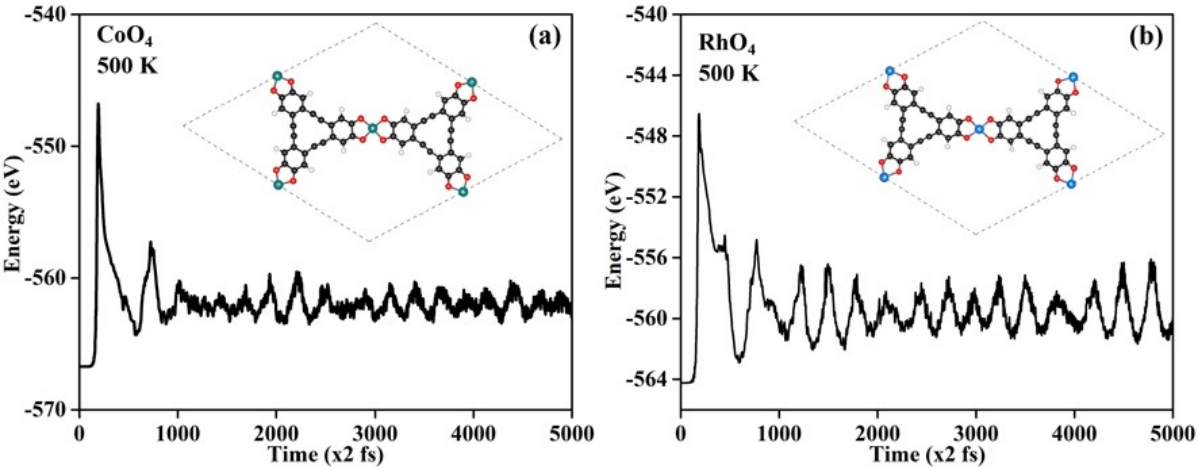

Fig. S22. Total energy variations of (a) CoO_4-HTC and (b) RhO_4-HTC as the function of time for AIMD simulation under 500 K condition. The snapshot of atomic configurations at the end of the AIMD simulation are inserted.

Table S1. The detailed average bond length between TM and N/O atoms change after different TM doping of TMN_xO_{4-x}-HTC catalysts. From the bond length between TM and N/O of all the designed TMN_xO_{4-x}-HTC catalysts, it can be concluded that the doping of different TM atoms on different N_xO_{4-x}-HTC substrates has impact on the bond length of adjacent TM-N and TM-O, mostly this is because the different atomic radii of TM and N/O atoms.

Catalysts	d_{TM-N} (Å)	d_{TM-O} (Å)	Catalysts	d_{TM-N} (Å)	d_{TM-O} (Å)
FeN_4	1.84	/	RhN_3O_1	1.91	1.97

CoN_4	1.82	/	PdN_3O_1	1.93	1.96
NiN_4	1.82	/	IrN_3O_1	1.92	1.96
RuN_4	1.92	/	PtN_3O_1	1.93	1.97
RhN_4	1.92	/	FeN_2O_2	1.85	1.85
PdN_4	1.93	/	CoN_2O_2	1.82	1.83
IrN_4	1.92	/	NiN_2O_2	1.82	1.83
PtN_4	1.93	/	RuN_2O_2	1.92	1.95
FeO_4	/	1.85	RhN_2O_2	1.91	1.96
CoO_4	/	1.83	PdN_2O_2	1.93	1.96
NiO_4	/	1.83	IrN_2O_2	1.91	1.95
RuO_4	/	1.96	PtN_2O_2	1.93	1.96
RhO_4	/	1.97	FeN_1O_3	1.85	1.85
PdO_4	/	1.98	CoN_1O_3	1.81	1.84
IrO_4	/	1.96	NiN_1O_3	1.81	1.85
PtO_4	/	1.98	RuN_1O_3	1.92	1.93
FeN_3O_1	1.84	1.86	RhN_1O_3	1.89	1.96
CoN_3O_1	1.81	1.85	PdN_1O_3	1.91	1.96
NiN_3O_1	1.82	1.85	IrN_1O_3	1.90	1.95
RuN_3O_1	1.95	2.00	PtN_1O_3	1.91	1.97

Table S2. For comparison, the calculated overpotentials for the OER (η^{OER}) and ORR (η^{ORR}) on the 2D-MOF materials are listed. The unit for η is V.

Catalysts	Methods	η^{OER}	η^{ORR}	Reference
$Ir_3(HITP)_2$	MS/DMol^3	/	0.31	[9]
$Rh_3(HITP)_2$	MS/DMol^3	/	0.37	[9]
Rh-HAB-CP	VASP/PBE	0.32	/	[10]
Fe-HAB-CP	VASP/PBE	/	0.52	[10]
$Rh_3(C_6O_6)_2$	VASP/PBE	/	0.36	[11]
FeIT	VASP/PBE	/	0.52	[12]
$Ir_3(HIB)_2$	MS/DMol^3	/	0.47	[13]

Co-CAT	MS/DMol^3	/	0.46	[14]
Co-pyridine-N_4	VASP/PBE	0.37	0.50	[15]
Co-N_4	MS/DMol^3	0.69	0.47	[16]
$Rh_3(C_6S_3O_3)_2$	VASP/PBE	/	0.42	[17]
CoN_3O_1	VASP/PBE	0.29	0.55	This work
RhN_2O_2	VASP/PBE	0.43	0.20	This work
RhO_4	VASP/PBE	0.33	0.39	This work

References

1 J.K. Nørskov, J. Rossmeisl, A. Logadottir and L. Lindqvist, Origin of the Overpotential for Oxygen Reduction at A Fuel-Cell Cathode, *J. Phys. Chem. B.* 2004, **108**, 17886-17892.

2 A. Valdes, Z.W. Qu and G.J. Kroes, Oxidation and Photo-Oxidation of Water on TiO_2 Surface, *J. Phys. Chem. C*. 2008, **112**, 9872-9879.

3 P. Atkins and J. Paula, J. Atkins' Physical Chemistry, Oxford University Press, 2014.

4 A.S. Feiner and A.J. McEvoy, The Nernst Equation, *J. Chem. Educ*., 1994, **71**, 493.

5 Y. Jiao, Y. Zheng, M. Jaroniec and S.Z. Qiao, Design of Electrocatalysts for Oxygen-and Hydrogen-Involving Energy Conversion Reactions, *Chem. Soc. Rev*., 2015, **44**, 2060.

6 H. Ma, X.Q. Chen, R.H. Li, S.L. Wang, J.H. Dong and W. Ke, First-Principles Modeling of Anisotropic Anodic Dissolution of Metals and Alloys in Corrosive Environments, *Acta Mater*., 2017, **130**, 137.

7 Z. Huang, J. Wang, Y. Peng, C. Jung, A. Fisher and X. Wang, Design of Efficient Bifunctional Oxygen Reduction/Evolution Electrocatalyst: Recent Advances and Perspectives, *Adv. Energy Mater*., 2017, **7**, 1700544.

8 B. Wei, Z.H. Fu, D. Legut, T.C. Germann, S.Y. Du, H.J. Zhang, J.S. Francisco and R.F. Zhang, Rational Design of Highly Stable and Active MXene-Based Bifunctional ORR/OER Double-Atom Catalysts, *Adv. Mater*., 2021, 2102595.

9 X. Chen, F.H. Sun, F. Bai and Z.F. Xie, DFT Study of the Two Dimensional Metal-Organic Frameworks $X_3(HITP)_2$ as the Cathode Electrocatalysts for Fuel Cell, *Appl. Surf. Sci*., 2019, **471**, 256-262.

10 G.P. Gao, E.R. Waclawik and A.J. Du, Computational Screening of Two-Dimensional Coordination Polymers as Efficient Catalysts for Oxygen Evolution and Reduction Reaction, *J. Catal*., 2017, **352**, 579-585.

11 J. Zhang, Z.P. Zhou, F. Wang, Y.F. Li and Y. Jing, Two-Dimensional Metal Hexahydroxybenzene Frameworks as Promising Electrocatalysts for an Oxygen Reduction Reaction, *ACS Sustainable Chem. Eng*., 2020, **8**, 7472-7479.

12 G.R. Xing, L. Cheng, K. Li, Y. Gao, H. Tang, Y. Wang and Z.J. Wu, A Density Functional Theory Study of the Two-Dimensional Bis(iminothiolato)metal Monolayers as Efficient Electrocatalysts for Oxygen Reduction Reaction, *J. Phys. Chem. C*., 2020, **124**, 7803-7811.

13 X.J. Yang, Q. Hu, X.L. Hou, J.L. Mi and P. Zhang, Oxygen Reduction Reaction on M_3(hexaiminobenzene)$_2$: A Density Function Theory Study, *Catal. Commun*., 2018, **115**, 17-20.

14 X. Chen, S.H. Huang, F.H. Sun and N.J. Lai, Modifications of Metal and Ligand to Modulate the Oxygen Reduction Reaction Activity of Two-Dimensional MOF Catalysts, *J. Phys. Chem. C*., 2020, **124**, 1413-1420.

15 H.X. Xu, D.J. Cheng, D.P. Cao and X.C. Zeng, A Universal Principle for A Rational Design of Single-Atom Electrocatalysts, *Nat. Catal*., 2018, **1**, 339-348.

16 X.L. Zhang, Z.X. Yang, Z.S. Lu and W. C. Wang, Bifunctional CoN_x Embedded Graphene Electrocatalysts for OER and ORR: A Theoretical Evaluation, *Carbon*., 2018, **130**, 112-119.

17 T.C. Li, M.M. Li, X.Y. Zhu, J. Zhang and Y. Jing, Conductive Two-Dimensional $M_3(C_6S_3O_3)_2$ Monolayers as Effective Electrocatalysts for the Oxygen Reduction Reaction, *J. Mater. Chem. A*., 2021, **9**, 24887-24894.